Laser pulse-length dependent ablation and shock generation in silicon at 5×10^{14} W/cm^2 intensities

M. Bailly-Grandvaux,[1,*] E. N. Hahn,[1] T. R. Joshi,[2] K. Werellapatha,[1] T. Cordova,[1] R. E. Turner,[1] J. E. Garay,[1] R. B. Spielman,[2] J. K. Wicks,[3] and F. N. Beg[1,†]

[1]*Center for Energy Research, University of California San Diego, La Jolla, California 92083, USA*
[2]*Laboratory for Laser Energetics, University of Rochester, Rochester, New York 14623, USA*
[3]*Department of Earth and Planetary Sciences, Johns Hopkins University, Baltimore, Maryland 21210, USA*

(Received 3 August 2022; accepted 20 May 2024; published 11 July 2024)

The effect of laser pulse duration on energy coupling into a planar silicon target is investigated in experiments at the OMEGA-EP facility by varying the laser pulse length τ—spanning 3 orders of magnitude from 100 ps to 10 ns—while maintaining a constant peak laser intensity, $I_0 = 5 \times 10^{14}$ W/cm^2. In theoretical models, the ablation pressure primarily scales for a given material with laser intensity and wavelength, which are all fixed variables here, allowing us to explore the specific role of laser pulse duration. Two-dimensional radiation-hydrodynamics simulations benchmarked with optical probing of the expanding plasma show that the pulse duration is critical for the ablation pressure to reach a steady state. Moreover, the pulse duration impacts shock decay and multiple wave effects, which strongly dictate the evolving shock profile that propagates within the laser-shocked target as ultimately measured by rear-surface diagnostics. The shock velocities inferred from the theoretical model, after considering shock decay, impedance matching, and shock Hugoniot, are found to be in good agreement with velocimetry measurements. However, discrepancies are observed with simulations for the shorter (0.1 ns) and longer (10 ns) pulse durations, which are respectively attributed to unaccounted contributions of kinetic absorption mechanisms and instabilities in simulations.

DOI: 10.1103/PhysRevResearch.6.033053

I. INTRODUCTION

There continues to be substantial interest in using high-intensity laser pulses as drivers for fusion schemes [1–4] and beyond as an experimental tool to create and probe high-energy density states of matter of interest to materials/shock physics [5,6], plasma physics [7], and astrophysics [8], among many other fields of study and applications [9,10]. Directed laser ablation begins in a thin absorption layer where the laser energy is transferred over femtoseconds to the target electrons through a variety of kinetic mechanisms including photoionization and impact ionization [11,12]. The amount of laser energy absorbed and the dominant absorption mechanisms are determined by target material and laser properties [11,13]. Following absorption of the laser energy, electrons begin transferring their energy to the material via electron-phonon and electron-ion collisions [12], causing the initial absorption layer to become superheated, and undergoing a number of possible phase transformations and failure mechanisms [14–16] that result in an expanding coronal plasma that forms above the target. After this fast initial ablation phase, laser energy at the studied intensity is primarily absorbed through inverse bremsstrahlung (IB) collisions [13,17] where the penetration of the laser beam is now limited by the critical plasma density, $n_c \approx 1.1 \times 10^{21}\ \lambda_{\mu m}^{-2}$ cm^{-3}, where $\lambda_{\mu m}$ is the laser wavelength in micrometers.

As the plasma expands away from the target, a pressure wave traveling in the opposite direction occurs as a result of a reaction force, often described as the "rocket effect," that imparts an ablation pressure on the underlying target [18]. The resulting thermomechanical shock (TMS) propagating forward has an initial strength that is determined by the amount of mass removed and the blow-off velocity [19]. A prominent real-world example of radiation-driven TMS is the threat experienced by exoatmospheric objects exposed to large fluxes of x rays. Specifically, the surface of many exoatmospheric objects contains critical surface electronics such as Si-based photovoltaic cells that may be exposed to high irradiation and TMS in the multi-Mbar regime during extreme events [20]. High-power lasers can be used as a surrogate to the large x-ray fluxes for such surface plasma ablation studies [21]. To establish a framework of comparison between the different sources of irradiation, it is first important to validate the scaling of ablation pressure with laser pulse parameters. In contrast to x-ray irradiation, the duration of the laser driver can modify the energy deposition location and coupling efficiency to the laser-ablated target [22], and consequently the shock generation and decay. Now, to the best of our knowledge, there are no data available in the literature benchmarking both laser ablation and shock propagation at high enough laser intensities and with a wide range of pulse durations, while keeping the intensity constant across the study, to make suitable comparisons with models

*Contact author: mbaillyg@ucsd.edu
†Contact author: fbeg@ucsd.edu

of ablation pressure to ultimately link the different sources of irradiation.

II. ABLATION

Here, we generated TMS in the laboratory using a direct laser drive to ablate an electronics surrogate multilayer target $Si/Cu/SiO_2$ (with thicknesses of 50, 25, and 500 μm, respectively). The silicon orientation was (100), the copper layer was 99.999% pure, and the quartz was z-cut. The specific objective of the work reported here is to characterize laser ablation and shock generation at a fixed intensity of $\sim 5 \times 10^{14}$ W cm^{-2} through experiments performed at the Omega EP laser facility [23] and relate the scaling of shock strength to the laser pulse length comparing data with radiation-hydrodynamic simulations and an analytical model. Note that the Cu layer was added to evaluate hot electron preheating. This specific analysis will be the object of future work. It is worth mentioning though that the dedicated diagnostics, namely, Cu $K_{\alpha,\beta}$ spectroscopy and the collection of backward stimulated Raman scattering (SRS) both show that the SRS activity and the hot electron preheating increase with pulse duration, which is a consequence of the increasing underdense plasma scale length.

A theoretical model relating the absorption of the incident laser pulse to the plasma was derived in 1982 by Mora [13], based principally on the contributions of IB absorption and the scale length of the plasma as related to the plasma critical density. Herein, scaling laws for the ablation pressure and temperature are derived with respect to the laser intensity (I), the wavelength (λ), and the pulse length (τ), as well as to the ratio of mass number to atomic number A/Z of the ablated material, each to specific powers.

The theoretical form proposed by Mora [13] for strong-bremsstrahlung absorption can be expressed as

$$P(\text{Mbar}) = 9.22\, I_{14}^{3/4} \lambda_{\mu m}^{-1/4} \left(\frac{A}{2Z}\right)^{7/16} (Z^* \tau_{ns} \ln \Lambda/6)^{-1/8}, \tag{1}$$

where Z^* is the ion charge state and $\ln \Lambda$ is the Coulomb logarithm. In what follows, we simply considered $\ln \Lambda = 6$, close to the value evaluated at the critical density of 0.351-nm light and ~1 keV electron temperature. Note that the intensity scaling exponent of 3/4 is related to a planar description of the plasma expansion. In this case, the model considers the self-similar expansion of a planar isothermal plasma with a density gradient scale length given by $L = c_s \tau$ [24], where c_s is the ion acoustic velocity of the expanding plasma. For $\tau = 1$ ns and at the critical density of 0.351-nm light and ~1 keV electron temperature, $L \sim 240$ μm. Here, we are indeed in a planar approximation since the scale length L does not largely exceed the focal spot diameter of ~1 mm. FLASH radiation-hydrodynamics simulations confirm this estimation (Table I) and indicate that L saturates to a maximum value of around 300 μm in a steady state.

To maintain a constant intensity of $\sim 5 \times 10^{14}$ W/cm^2 while varying the pulse length, the energy delivered on target is varied from 200 J to 20 kJ split between two and four overlapping $\lambda = 0.351$ μm beams with phase plates modulating the on target spot-size radius to be $r \sim 500$ μm (90% enclosed energy). A sketch of the experimental setup is presented in Fig. 1. Errors expected from focusing, pointing, and spatial differences in the phase plates are expected to be minimal, placing the expected error in delivered intensity to be less than $\sim 1.5 \times 10^{14}$ W/cm^2. In such experiments aiming at validating ablation physics and shock propagation models, it is worth pointing out the importance to employ large focal spots and smoothing techniques to alleviate two-dimensional (2D) effects, otherwise causing complex lateral flows of energy and mass in the targets [25].

TABLE I. Average electron temperatures (T_e) and scale length ($L = n_e/\nabla n_e$) from the 2D radiation-hydrodynamics FLASH simulations at $\sim n_{c,3\omega}/4$ at three characteristic timings (0.5, 1, and 2 ns).

	$t = 0.5$ ns		$t = 1.0$ ns		$t = 2.0$ ns	
τ (ns)	T_e (keV)	L (μm)	T_e (keV)	L (μm)	T_e (keV)	L (μm)
0.1	0.7	14.3	0.4	9.1	0.03	19.5
0.5	2.2	58.6	1.4	168.6	0.35	29.95
1	2.1	58.6	2.5	128.3	1.1	227.9
10	2.0	53.4	2.5	125.0	2.9	269.6

The theoretical ablation pressure predicted from Eq. (1) for $\tau = 1$ ns is ~25 Mbar. Besides the pulse duration dependence due to delocalized absorption, this same equation importantly highlights the strong scaling expected with laser intensity and wavelength, as similarly reported by other experimental studies and models [18,25,26]. With respect to τ, increasing the pulse length to 10 ns should decrease the ablation pressure by 25% and decreasing the pulse length to 100 ps should increase the ablation pressure by 33% according to the theoretical scaling.

A primary diagnostic of the experiments was selected to characterize the 2D (axial and radial) coronal plasma

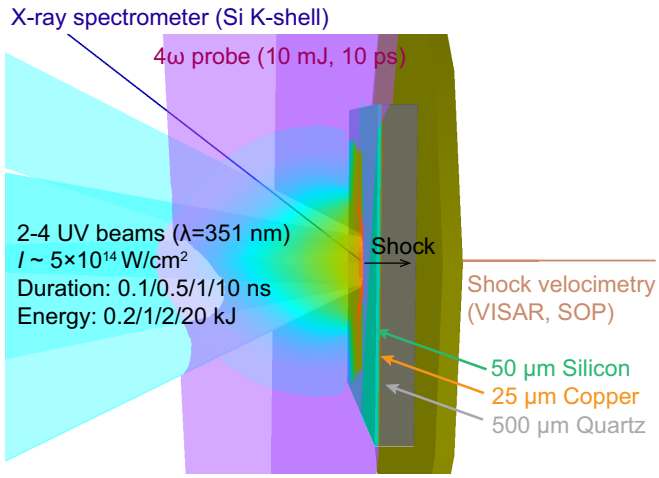

FIG. 1. Sketch of the experimental setup. The streaked optical pyrometer (SOP) and a velocity interferometer system for any reflector (VISAR) are used to measure the shock breakout time and to track shock fronts or interfaces moving in the target, respectively. The 4ω probe with angular filter refractometry measures the density distribution of the Si ablated plasma. The Si ablator K-shell emission is recorded with a time-integrated spectrometer, which provides a measurement of the peak plasma temperature near the ablated target surface.

density profiles at a specific snapshot in its evolution using the 4ω probe and angular filtered refractometry (AFR) [27]. The 10-ps, 10-mJ, 4ω probe refracts as it propagates through the undercritical ($n_e < n_c$) ablated plasma, with $n_{c,4\omega} = 1.6 \times 10^{22}$ cm^{-3} being the critical density at the probe wavelength $\lambda_{4\omega} = 263$ nm. The probe's total phase accrued from propagating in the plasma is filtered at the unrefracted probe beam focus (i.e., the Fourier plane) by alternating rings of opaque and transparent sections, and then it is collected to an image plane at $f/4$.

The probe refraction is directly proportional to the radial position in the Fourier plane. Hence, the shadow bands resulting from the filter are contours of constant refraction. The resultant image is a contour map of the refraction angles of the probe beam. Details of this diagnostic are presented in Refs. [27,28]. The refraction angle of the probe rays is proportional to the gradient of the probe phase after passing through the plasma:

$$\theta_{4\omega}(x, y) = \frac{\lambda_{4\omega}}{2\pi} |\vec{\nabla}\phi(x, y)|, \tag{2}$$

$$\text{where} \quad \phi(x, y) = \frac{\pi}{\lambda_{4\omega} n_{c,4\omega}} \int_{-\infty}^{\infty} n_e(x, y, z) dz, \tag{3}$$

Rather than performing an inversion of the phase measurement to retrieve the path-integrated density, it is more common to process analytical and simulated density profiles for direct comparison with the experimental data.

We performed 2D radiation-hydrodynamic simulations in cylindrical geometry ($r - z$) using FLASH [29,30], with the laser ray-tracing utilizing FLASH's 3D-in-2D model for laser energy deposition. In FLASH, the laser energy deposition is calculated solely from IB, being delivered here by one equivalent laser source (rather than the two or four used in the experiments). Tabulated equation of state (EOS) models were generated for the target layers (silicon, copper, quartz) using PrOpacEOS [31]. Taking advantage of the axial symmetry, a synthetic AFR image can be generated from the reconstructed 3D profile of density. This procedure allows for a validation of the simulated plasma ablation in FLASH, which can then be leveraged to infer the evolution of the ablated plasma at times not experimentally probed.

Figure 2 shows an overlay of experimental and synthetic (postprocessed from FLASH simulations) AFR images for the 1-ns-pulse configuration at successive times through the ablated plasma's evolution: 0.5 ns (a), 1.5 ns (b), and 2 ns (c), and for other pulse durations, 0.1 ns (d), 0.5 ns (e), and 10 ns (f), at a fixed probing time of 2 ns. Note that the experimental AFR images were also benchmarked to FLASH simulations using analytical fits, according to Ref. [32]. We observed a relatively good agreement with the experiment across the explored timings and pulse lengths. Note though that differences emerge when probing the coronal plasma after the laser turns off (free expansion).

The overall agreement of the ablated plasma's scale and growth provides confidence in the simulated plasma evolution and gives insight into the experimental conditions. For $\tau = 1$ ns, the electron temperature peaks at $T_e \sim 2200$ eV in the region $n_{c,3\omega}/4 - n_{c,3\omega}/10$, where $n_{c,3\omega} = 8.9 \times 10^{21}$ cm^{-3} of the UV ($\lambda_{3\omega} = 351$ nm) driving laser. The simulated

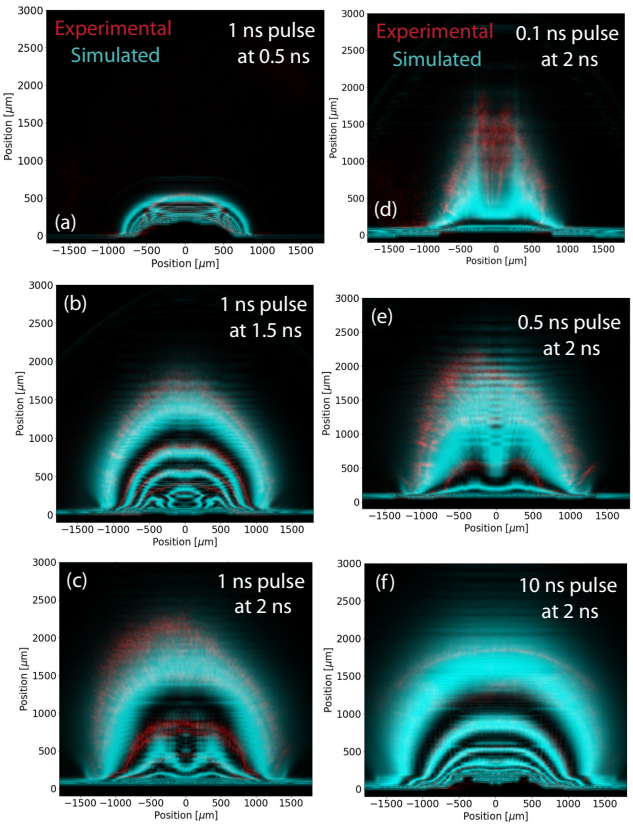

FIG. 2. Comparison (overlay) of experimental and synthetic (postprocessed from FLASH simulations) AFR images, showing the ablated plasma evolution for the 1-ns-pulse setup at the probe times (a) 0.5 ns, (b) 1.5 ns, and (c) 2 ns, and for other pulse durations, 0.1 ns (d), 0.5 ns (e), and 10 ns (f), at a probing time of 2 ns. Note that the central artifact in simulated AFR images is a consequence of the 3D reconstruction of the cylindrical $r - z$ simulations near $r = 0$.

average electron temperatures and plasma scale lengths in the underdense coronal plasma at 0.5, 1, and 2 ns for all pulse durations are reported in Table I.

Generally, the effect of longer laser pulses shows two prominent features: more ablated material and therefore longer density scale lengths in the $n_{c,3\omega}/4$ to $n_{c,3\omega}/10$ region, as well as significantly higher temperatures over the longer timescale. Specifically, at 2 ns for the 0.1-ns pulse, we can infer from the simulation profiles an average electron temperature of $T_e \sim 0.03$ keV. For the remaining configurations at $t = 2$ ns, the temperature increases with the pulse length: $T_e \sim 0.35$, 1.1, and 2.9 keV for the 0.5-, 1-, and 10-ns pulses, respectively. The lower temperatures for shorter pulse lengths are not unexpected, as only the $\tau = 10$ ns pulse is still active at 2 ns. Comparing the four pulses at 1 ns after laser ablation reveals a remarkable self-similarity in electron temperature for the two pulse lengths that are still active (1 and 10 ns), with $T_{e,1\,\mathrm{ns}(1\,\mathrm{ns})} \sim 2.6$ keV and $T_{e,10\,\mathrm{ns}(1\,\mathrm{ns})} \sim 2.5$ keV. Moving further back in time to 0.5 ns when three out of four cases are still actively ablating, $T_{e,0.5\,\mathrm{ns}(0.5\,\mathrm{ns})} \sim 2.2$ keV, $T_{e,1\,\mathrm{ns}(0.5\,\mathrm{ns})} \sim 2.1$ keV, and $T_{e,10\,\mathrm{ns}(0.5\,\mathrm{ps})} \sim 2.0$ keV, and for the 0.1-ns pulse $T_{e,0.1\,\mathrm{ns}(0.5\,\mathrm{ns})} \sim 0.7$ keV. Effectively, the 0.5-, 1-, and 10-ns pulses show impressive self-similarity over the

TABLE II. Electron temperature inferred from silicon spectroscopy (using Ly_γ/He_γ line intensity ratio or continuum emission) emitted at an estimated electron density of 3×10^{22} cm^{-3} (using Stark broadening theory on line widths). The values are compared to radiation-hydrodynamics simulations (FLASH) at the inferred density and at the end of each pulse ($t = \tau$).

	T_e (eV) at $n_e = 3 \times 10^{22}$ cm^{-3}		
τ (ns)	Si Ly_γ/He_γ	Si continuum emission	FLASH at $t = \tau$
0.1	428 ± 52	468 ± 47	351
0.5	500 ± 60	460 ± 46	553
1	494 ± 60	458 ± 46	508
10	495 ± 60	500 ± 50	580

duration of time for which each pulse is active, after which the temperature of the coronal plasma begins to cool rapidly. Comparing the scale length L for $\tau > 0.5$ ns we find similarity that persists after laser turn off, with values of ~200–300 μm in the coronal plasma away from the target.

Electron temperatures of the ablation front region were experimentally measured using a time-integrated Rowland x-ray spectrometer (XRS) [33] designed to measure emissions in the spectral range of 1.8 to 3.5 KeV where Si K-shell line emission occurs. We specifically compare optically thin (optical depth $\leqslant 1$) $Ly_\gamma(4p - 1s; 2506$ eV) and $He_\gamma(1s4p - 1s2; 2292$ eV) line intensity ratios with atomic kinetics calculations using PRISMSPECT [34], taking into account the instrumental resolution of $E/\Delta E \sim 300$ [33]. Electron densities were also inferred by fitting data with the synthetic spectra computed via PRISMSPECT. The fitted spectra provide an electron density estimate (through Stark broadening) of $\sim 3 \times 10^{22}$ cm^{-3}, which corresponds to a thin (<10 μm) plasma layer located above the solid target surface that dominates the emission because it is both hot and dense. The electron temperature was also estimated from the slope of continuum emission in the photon energy range of ~7–10 keV recorded by a von Hamos spectrometer [35]. Table II reports the electron temperatures measured using the two independent spectroscopic techniques and compared with radiation-hydrodynamics simulations for all pulse lengths. The electron temperature is extracted from the simulations at the end of each pulse and at the previously inferred density, to provide a meaningful comparison to the space- and time-integrated measurements. In simulations, including the longest 10-ns pulse duration, we indeed observe that the temperature starts decreasing immediately after the laser pulse ends, but not before. For $\tau = 0.1$ ns, the measured electron temperature is 428 ± 52 eV and for all other cases, the measured electron temperature is ~500 eV. From the FLASH simulations, we extract a similar temperature of ~500 eV at this density, just before the laser turns off, which is in good agreement with spectroscopy measurements.

III. SHOCK GENERATION

Ultimately, the aforementioned energy transfer between the laser and coronal plasma will support a driving pressure on the underneath target. If the ablation pressure is of sufficient

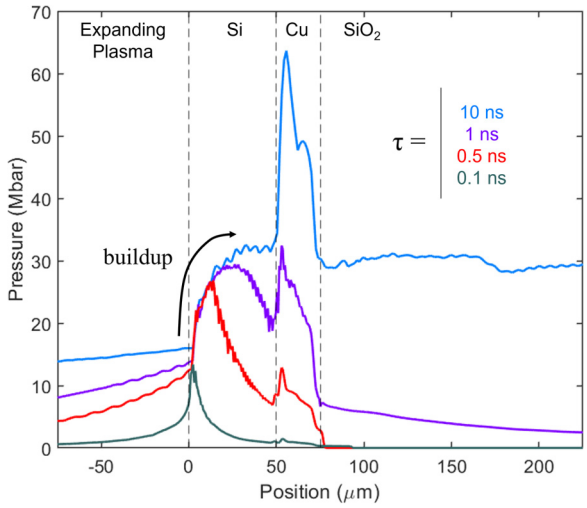

FIG. 3. Maximum pressure (ablation/shock) evolution as a function of position simulated from the FLASH simulation for each pulse duration.

magnitude, the resultant wave will shock up and traverse deeper into the target. This is directly visualized from the FLASH simulations in Fig. 3 where the maximum pressure evolution in each zone is plotted as a function of position near the target surface (initially at $z = 0$) with the laser drive propagating from left to right.

The self-similarity of the pulses can be observed from the position in the Si material where ablation pressure is piling up near the target surface. Each case with $\tau \leqslant 1$ ns displays a characteristic beam turn-off point after which the pressure begins to decay rapidly. As Fig. 3 is a spatial plot, we can see that the point where the decay occurs has propagated farther in depth with increasing pulse duration. For $\tau = 10$ ns, the beam remains on for the entirety of the simulation: the pressure wave is supported deep into the target. The peak ablation pressures increase with increasing pulse length reaching ~13, ~27, and ~29 Mbar, for 100 ps, 500 ps, and 1 ns accordingly, while the 10-ns pulse observes a steady ablation pressure of ~32 Mbar. A closer look at Fig. 3 suggests that the critical time to develop a steady ablation pressure is ~1 ns. We also observe that while the ablation pressures are in ballpark agreement with Eq. (1) for 0.5- and 1-ns pulses, with a difference of less than 20%. The difference increases to about 45% for the 10-ns pulse and to about 60% for the 0.1-ns pulse, with an opposite trend with pulse duration compared to the delocalized absorption effect predicted by Eq. (1). This discrepancy will be discussed after the comparison with measured shock velocities, giving more insights into the origin of this disagreement.

Also evident in Fig. 3 is the complex trajectory of the shock wave through the target, where the pressure increases in the Cu layer and decreases again as it transits into the SiO_2 (single-crystal quartz) witness layer. This is due to impedance effects at the target layers' interfaces [36]. Moreover, as the shock wave progresses from the surface into the depth of the target, the pressure will decay [37]. This effect is magnified for short-duration pulses where the shock wave is unsupported and dispersion also occurs laterally from the laser spot toward the edge of the samples. However, note that the experimental

thickness-to-width ratio is ∼1:6; thus, any side reflections from the edge of the sample will occur long after the diagnostic acquisition time window.

Two related diagnostics, streaked optical pyrometry (SOP) [38] and velocimetry interferometer system for any reflector (VISAR) [39], are used to infer the strength of the shock in the target. SOP and VISAR probe the optically transparent quartz (SiO_2) witness layer. If the shock strength is in excess of a few Mbar, it transforms the SiO_2 material from a dielectric to an opaque conducting material, making the optical probing depth ≪100 nm, and thus both diagnostics effectively probe the evolving shock front as it progresses [40]. SOP measures the self-emission of the hot shock front, whereas VISAR utilizes the Doppler effect of an illuminating laser probe to infer changes in velocity of the shock interface (U_s). Both diagnostics give a direct measure of the shock break-out time (SBO) or the time at which the shock first transits into the SiO_2, in addition to time-resolved data after that. The intensity of the SOP emission can be correlated with the shock-induced temperature rise, and thus the shock velocity as well [38], giving two measurements of the time-dependent shock velocity in the SiO_2.

Shown in Fig. 4 are the FLASH-simulated $x-t$ of the local maximum pressure in panel (a) and maximum particle velocity in panel (b), as well as a direct comparison of the shock velocity in SiO_2 between the FLASH simulation and the SOP and VISAR time-resolved data, for $\tau = 1$ ns. The measured and simulated shock velocities at the Cu/SiO_2 interface for other pulse lengths are summarized further in Fig. 5. In the $x-t$ maps of Fig. 4, time evolves from top to bottom, and depth is shown from left to right, the same as the laser direction. The sharp pressure increase observed in the Cu layer in Fig. 4(a) is due to the expected impedance effects as the shock transits from the Si layer to the Cu layer and then from the Cu layer to the SiO_2 layer.

Ultimately, we would like to relate the theoretical ablation pressure [Eq. (1)] that occurs at the irradiated Si layer to the shock strength measured in the SiO_2; thus, we must account for the path-dependent evolution of pressure through the multilayer target. An impedance matching technique [36] is used, accounting for the shock Hugoniot of the Si [41]/Cu [42]/SiO_2 [40,43] layers, respectively. For a shock pressure of ∼30 Mbar, approximately ∼128% and ∼64% of the pressure transfers across each interface, resulting in ∼82% of the ablation pressure translated to the SiO_2 layer. Notably, the shock propagation from the Cu to the SiO_2 layer also results in ∼36% reflection, which causes multiple secondary wave effects that reverberate within the Cu layer, as evidenced in Fig. 4(b).

Using experimental data from $\tau = 0.5$ ns and $\tau = 1$ ns, we are able to fit the decaying shock velocity within the SiO_2 layer as follows:

$$U_s(t) = U_s(\mathrm{SBO})e^{-t/4}, \tag{4}$$

where SBO is the shock breakout time at the Cu/SiO_2 interface.

We can also analytically predict that the leading edge of the rarefaction wave generated when the laser turns off will catch the shock front and cause decay at approximately 2τ [44,45]. Knowing the expected time for the beginning of shock decay is useful because decay that occurs before the shock breaks out will cause a decrease in measured U_s at the Cu/SiO_2 interface. Thus, the exponent in Eq. (4) effectively becomes $\frac{1}{4}(\mathrm{SBO} - 2\tau)$ for pulse lengths with SBO $>2\tau$ and no decay is expected if SBO $<2\tau$. Note here that the SBO time is directly related to the thickness of the multilayer target above the SiO_2 witness.

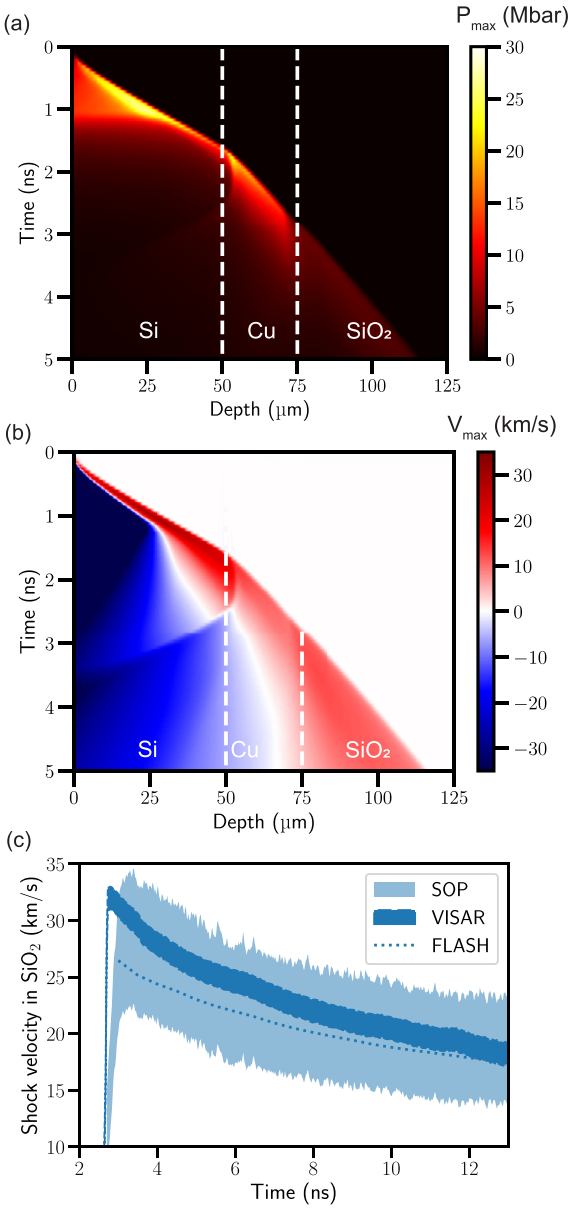

FIG. 4. Simulated $x-t$ evolution of the local maximum pressure (a) and maximum particle velocity (b) in the 2D radiation-hydrodynamics FLASH simulations for $\tau = 1$ ns. The corresponding simulated time evolution of the shock velocity in SiO_2 is displayed with a blue dashed line in panel (c) and compared to SOP (light blue) and VISAR (dark blue) measurements.

Using Eq. (1) without the pulse length term, (i.e., fixing τ to 1 ns), applying the expected impedance matching and decay effects, and using the experimentally measured SBO shown in Fig. 5(b), we obtain an analytical prediction of shock velocity measured at the Cu/SiO_2 interface as a function of pulse length. Note that the pulse-length dependence

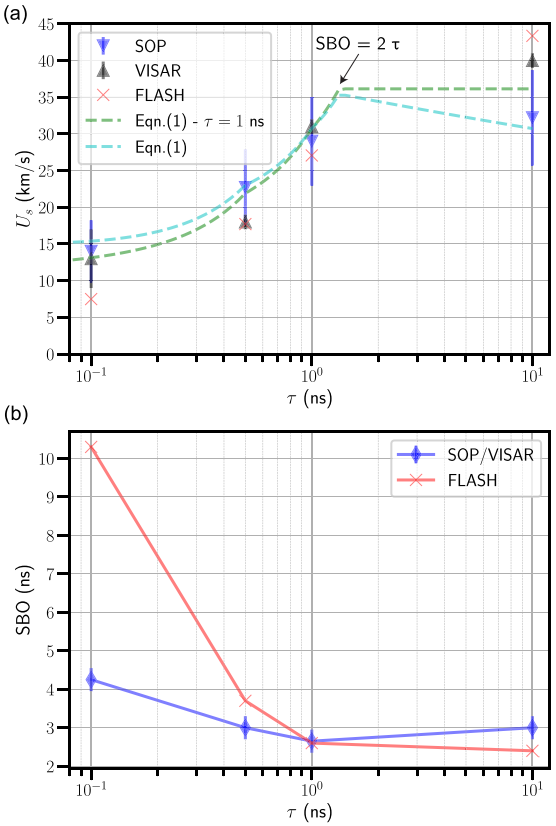

FIG. 5. (a) Shock velocity (U_s) measured at the Cu/SiO_2 interface. The two dashed lines in panel (b) are derived from Eq. (1), accounting for shock Hugoniot, decay effects, and impedance matching, fixing τ to 1 ns (green dashed line) or including the τ dependence in this same equation (cyan dashed line). (b) Shock break-out time at the Cu/SiO_2 interface.

in this case solely arises from the shock decay [Eq. (4)]. This prediction is plotted with a green dashed line in Fig. 5 in comparison to average values extracted from SOP and VISAR measurements (blue and black triangles, respectively). The error bars result, for SOP, from the uncertainty of the reflection coefficient in the gray-body approximation and background subtraction [38,39], and for VISAR, they result from the phase uncertainty evaluated to a conservative $\pm 10\%$ of the velocity-per-fringe constant [46], also accounting for shot-to-shot variations. Note that in Fig. 4(c), error bars were calculated identically.

Interestingly, Fig. 5(a) shows that the theoretical model intersects the data within error bars. However, including the pulse duration dependence from Eq. (1) [cyan dashed line in Fig. 5(a)] is shown to similarly intersect the data within error bars. Overall, the pulse duration dependence in Eq. (1) does not yield strong enough differences in the shock velocities to be discriminated against our experimental measurements. On the other hand, this analysis shows that the effect of pulse duration on shock decay [Eq. (4)] is critical to the accuracy of the analytical modeling.

Finally, in the plots of shock velocity [Fig. 5(a)] and SBO [Fig. 5(b)] at the Cu/SiO_2 interface, the results from the FLASH radiation-hydrodynamics simulations are shown with red cross symbols. The comparison with experimental data shows a good agreement for $\tau \sim 1$ ns for both SBO and shock velocities, but discrepancies are observed for the shortest (0.1 ns) and longest (10 ns) pulse lengths, with clear differences already observed in the evaluation of the SBO time [Fig. 5(b)]. Interestingly, the laser energy absorption efficiency in FLASH is evaluated to be 15%, 30%, 40%, and 95%, respectively for the 0.1-, 0.5-, 1-, and 10-ns pulses. In Fig. 1 of Ref. [47], the authors reported measured absorption fractions of laser light as a function of incident intensity for various experimental conditions, including a comparison between 80-ps and 2-ns pulses at a 0.53-μm wavelength. While the total energy (or fluence) in the pulses used in this study is about a 1000 times lower than in our experiment, such that an absolute comparison would be misleading; it shows that the absorption efficiency from 2-ns to 80-ps pulses is reduced by $<20\%$ at constant intensity, in contrast to the factor ~ 2.5 reduction seen in our simulations between 1-ns and 100-ps pulses. Remarkably, despite the simplifications and assumptions used in the analytical model, excluding, for instance, the consideration of varying laser absorption efficiency with laser pulse duration, Fig. 5 shows that the shock velocities U_s inferred from the model are in good agreement with measurements for all explored pulse lengths. Therefore, it is clear that absorption efficiencies in simulations for the shortest pulse (and to a lesser extent, the longest pulse) are inaccurate, at least without artificially tuning the energy coupling in simulations. To better understand this discrepancy, it is important to recall that the active laser energy transfer physics in hydrodynamic codes (including FLASH) is limited to IB. For short pulse lengths, collisionless and skin-depth absorption mechanisms [48] are absent, while they are expected to have an increasing role over IB on timescales of femtoseconds to hundreds of picoseconds, especially in silicon with an expected absorption layer of <10 nm for 351-nm light. This leads to an underprediction of energy transfer for the 100-ps case. On the other hand, for multi-nanosecond timescales, with the presence of long density gradients, nonlinear absorption mechanisms such as parametric instabilities [49] take energy out of the laser electromagnetic wave, and the laser coupling efficiency with the critical density is thus overestimated in simulations for long pulse duration.

IV. CONCLUSIONS

In conclusion, we saw that theoretical scaling is in good agreement with measured shock velocities at the Cu/SiO_2 interface when accounting for shock decay and impedance matching. Moreover, the ablated plasma evolution inferred from 2D radiation-hydrodynamics simulations matches well with the measurements. However, while showing a similar trend and a good agreement for $\tau \sim 1$ ns pulses, simulations fail to quantitatively reproduce the SBO times and shock velocities for $\tau = 0.1$ ns and $\tau = 10$ ns, which are respectively attributed to unaccounted contributions of kinetic absorption mechanisms and instabilities in the standard treatment of hydrodynamics simulations. On the other hand, when considering the role of pulse duration in laser ablation and subsequent shock physics, our findings show that the main effects are seen through the occurrence of a shock decay after 2τ, in addition to a time-dependent buildup of ablation pressure that occurs on the several-nanosecond timescale below the critical surface. Such findings are important to

experiments aiming at using the shock information to test, for instance, material properties or equations of states under intense laser-based compression [50]. It is also worth mentioning that our study is performed at a laser intensity (10^{14}–10^{15} W/cm^2) and a wavelength (3ω, 0.351 nm) that are of interest to laser implosion experiments for inertial confinement fusion and other high-energy-density physics studies.

ACKNOWLEDGMENTS

The data that support the findings of this study are available upon request from the corresponding author, M.B.G.

The authors thank the technical support staff of LLE for help with the laser operation and plasma diagnostics. The authors also thank M. Millot and M. Marshall for assistance in SOP and VISAR analyses. This material is based upon work supported by the Defense Threat Reduction Agency under Award No. HDTRA12020001. Discussions among the Materials Science in Extreme Environments RA4–Photon-Material Interactions group aided in developing the technical content of the present work. This work was supported by DOE Office of Science, Fusion Energy Sciences under Contract No. DE-SC0021061: the LaserNetUS initiative at the OMEGA EP Laser Facility.

[1] R. Kodama, P. A. Norreys, K. Mima, A. E. Dangor, R. G. Evans, H. Fujita, Y. Kitagawa, K. Krushelnick, T. Miyakoshi, N. Miyanaga *et al.*, Fast heating of ultrahigh-density plasma as a step towards laser fusion ignition, Nature **412**, 798 (2001).

[2] L. J. Perkins, R. Betti, K. N. LaFortune, and W. H. Williams, Shock ignition: A new approach to high gain inertial confinement fusion on the national ignition facility, Phys. Rev. Lett. **103**, 045004 (2009).

[3] J. R. Davies. D. H. Barnak. R. Betti, E. M. Campbell, P.-Y. Chang, A. B. Sefkow, K. J. Peterson, D. B. Sinars, and M. R. Weis, Laser-driven magnetized liner inertial fusion, Phys. Plasmas **24**, 062701 (2017).

[4] R. H. H. Scott, K. Glize, L. Antonelli, M. Khan, W. Theobald, M. Wei, R. Betti, C. Stoeckl, A. G. Seaton, T. D. Arber *et al.*, Shock ignition laser-plasma interactions in ignition-scale plasmas, Phys. Rev. Lett. **127**, 065001 (2021).

[5] B. A. Remington, R. E. Rudd, and J. S. Wark, From microjoules to megajoules and kilobars to gigabars: Probing matter at extreme states of deformation, Phys. Plasmas **22**, 090501 (2015).

[6] D. C. Swift, T. E. Tierney IV, R. A. Kopp, and J. T. Gammel, Shock pressures induced in condensed matter by laser ablation, Phys. Rev. E **69**, 036406 (2004).

[7] F. Fiúza, A. Stockem, E. Boella, R. A. Fonseca, L. O. Silva, D. Haberberger, S. Tochitsky, C. Gong, W. B. Mori, and C. Joshi, Laser-driven shock acceleration of monoenergetic ion beams, Phys. Rev. Lett. **109**, 215001 (2012).

[8] A. Ciardi, T. Vinci, J. Fuchs, B. Albertazzi, C. Riconda, H. Pépin, and O. Portugall, Astrophysics of magnetically collimated jets generated from laser-produced plasmas, Phys. Rev. Lett. **110**, 025002 (2013).

[9] J. Ion, *Laser Processing of Engineering Materials: Principles, Procedure and Industrial Application* (Elsevier, Amsterdam, 2005).

[10] T. Nakamura, J. K. Koga, T. Z. Esirkepov, M. Kando, G. Korn, and S. V. Bulanov, High-power γ-ray flash generation in ultraintense laser-plasma interactions, Phys. Rev. Lett. **108**, 195001 (2012).

[11] A. M. Komashko, *Laser-Material Interaction of Powerful Ultrashort Laser Pulses* (University of California, Davis, 2003).

[12] E. G. Gamaly and A. V. Rode, Physics of ultra-short laser interaction with matter: From phonon excitation to ultimate transformations, Prog. Quantum Electron. **37**, 215 (2013).

[13] P. Mora, Theoretical model of absorption of laser light by a plasma, Phys. Fluids **25**, 1051 (1982).

[14] A. Cavalleri, K. Sokolowski-Tinten, J. Bialkowski, M. Schreiner, and D. von der Linde, Femtosecond melting and ablation of semiconductors studied with time of flight mass spectroscopy, J. Appl. Phys. **85**, 3301 (1999).

[15] L. V. Zhigilei and B. J. Garrison, Mechanisms of laser ablation from molecular dynamics simulations: dependence on the initial temperature and pulse duration, Appl. Phys. A **69**, S75 (1999).

[16] J. Bonse, S. Baudach, J. Krüger, W. Kautek, and M. Lenzner, Femtosecond laser ablation of silicon–modification thresholds and morphology, Appl. Phys. A **74**, 19 (2002).

[17] N. Farid, S. S. Harilal, H. Ding, and A. Hassanein, Emission features and expansion dynamics of nanosecond laser ablation plumes at different ambient pressures, J. Appl. Phys. **115**, 033107 (2014).

[18] J. Lindl, Development of the indirect-drive approach to inertial confinement fusion and the target physics basis for ignition and gain, Phys. Plasmas **2**, 3933 (1995).

[19] B. Yaakobi, T. Boehly, P. Bourke, Y. Conturie, R. S. Craxton, J. Delettrez, J. M. Forsyth, R. D. Frankel, L. M. Goldman, R. L. McCrory *et al.*, Characteristics of target interaction with high power UV laser radiation, Opt. Commun. **39**, 175 (1981).

[20] W. J. Karzas and R. Latter, Detection of the electromagnetic radiation from nuclear explosions in space, Phys. Rev. **137**, B1369 (1965).

[21] C. Osolin, NIF's laser energy will test nuclear survivability in space, Report, LLNL, 2021, https://lasers.llnl.gov/news/nifs-laser-energy-will-test-nuclear-survivability-in-space.

[22] L. Zhou, X.-Y. Li, W.-J. Zhu, J.-X. Wang, and C.-J. Tang, The effects of pulse duration on ablation pressure driven by laser radiation, J. Appl. Phys. **117**, 125904 (2015).

[23] L. J. Waxer, D. N. Maywar, J. H. Kelly, T. J. Kessler, B. E. Kruschwitz, S. J. Loucks, R. L. McCrory, D. D. Meyerhofer, S. F. B. Morse, C. Stoeckl *et al.*, High-energy petawatt capability for the omega laser, Opt. Photonics News **16**, 30 (2005).

[24] P. Mora and R. Pellat, Self-similar expansion of a plasma into a vacuum, Phys. Fluids **22**, 2300 (1979).

[25] D. Batani, H. Stabile, A. Ravasio, G. Lucchini, F. Strati, T. Desai, J. Ullschmied, E. Krousky, J. Skala, L. Juha *et al.*, Ablation pressure scaling at short laser wavelength, Phys. Rev. E **68**, 067403 (2003).

[26] W. M. Manheimer, D. G. Colombant, and J. H. Gardner, Steady-state planar ablative flow, Phys. Fluids **25**, 1644 (1982).

[27] D. Haberberger, S. Ivancic, S. X. Hu, R. Boni, M. Barczys, R. S. Craxton, and D. H. Froula, Measurements of electron density

profiles using an angular filter refractometer, Phys. Plasmas **21**, 056304 (2014).

[28] P. V. Heuer, D. Haberberger, S. T. Ivancic, C. Dorrer, C. A. Walsh, and J. R. Davies, Improved filters for angular filter refractometry, Rev. Sci. Instrum. **95**, 023501 (2024).

[29] D. R. Farley, K. Shigemori, and H. Azechi, Laser-produced blast wave and numerical simulation using the flash code, Laser Part. Beams **23**, 513 (2005).

[30] A. C. Calder, B. Fryxell, T. Plewa, R. Rosner, L. J. Dursi, V. G. Weirs, T. Dupont, H. F. Robey, J. O. Kane, B. A. Remington *et al.*, On validating an astrophysical simulation code, Astrophys. J., Suppl. Ser. **143**, 201 (2002).

[31] J. MacFarlane, I. Golovkin, and P. Woodruff, HELIOS-CR – A 1-D radiation-magnetohydrodynamics code with inline atomic kinetics modeling, J. Quant. Spectrosc. Radiat. Transfer **99**, 381 (2006).

[32] P. Angland, D. Haberberger, S. T. Ivancic, and D. H. Froula, Angular filter refractometry analysis using simulated annealing, Rev. Sci. Instrum. **88**, 103510 (2017).

[33] D. B. Thorn, F. Coppari, T. Döppner, M. J. MacDonald, S. P. Regan, and M. B. Schneider, X-ray spectrometer throughput model for (selected) flat Bragg crystal spectrometers on laser plasma facilities, Rev. Sci. Instrum. **89**, 10F119 (2018).

[34] J. J. MacFarlane, I. E. Golovkin, P. Wang, P. R. Woodruff, and N. A. Pereyra, SPECT3D – A multi-dimensional collisional-radiative code for generating diagnostic signatures based on hydrodynamics and PIC simulation output, High Energy Density Phys. **3**, 181 (2007).

[35] L. C. Jarrott, M. S. Wei, C. McGuffey, F. N. Beg, P. M. Nilson, C. Sorce, C. Stoeckl, W. Theoboald, H. Sawada, R. B. Stephens, P. K. Patel, H. S. McLean, O. L. Landen, S. H. Glenzer, and T. Döppner, Calibration and characterization of a highly efficient spectrometer in von Hamos geometry for 7–10 keV x-rays, Rev. Sci. Instrum. **88**, 043110 (2017).

[36] M. A. Meyers, *Dynamic Behavior of Materials* (Wiley & Sons, New York, 1994).

[37] M. Millot, Identifying and discriminating phase transitions along decaying shocks with line imaging Doppler interferometric velocimetry and streaked optical pyrometry, Phys. Plasmas **23**, 014503 (2016).

[38] M. C. Gregor, R. Boni, A. Sorce, J. Kendrick, C. A. McCoy, D. N. Polsin, T. R. Boehly, P. M. Celliers, G. W. Collins, D. E. Fratanduono *et al.*, Absolute calibration of the omega streaked optical pyrometer for temperature measurements of compressed materials, Rev. Sci. Instrum. **87**, 114903 (2016).

[39] S. Brygoo, M. Millot, P. Loubeyre, A. E. Lazicki, S. Hamel, T. Qi, P. M. Celliers, F. Coppari, J. H. Eggert, D. E. Fratanduono *et al.*, Analysis of laser shock experiments on precompressed samples using a quartz reference and application to warm dense hydrogen and helium, J. Appl. Phys. **118**, 195901 (2015).

[40] M. Millot, N. Dubrovinskaia, A. Černok, S. Blaha, L. Dubrovinsky, D. G. Braun, P. M. Celliers, G. W. Collins, J. H. Eggert, and R. Jeanloz, Shock compression of stishovite and melting of silica at planetary interior conditions, Science **347**, 418 (2015).

[41] B. Henderson, M. C. Marshall, T. R. Boehly, R. Paul, C. A. McCoy, S. X. Hu, D. N. Polsin, L. E. Crandall, M. F. Huff, D. A. Chin *et al.*, Shock-compressed silicon: Hugoniot and sound speed up to 2100 GPa, Phys. Rev. B **103**, 094115 (2021).

[42] C. A. McCoy, M. D. Knudson, and S. Root, Absolute measurement of the Hugoniot and sound velocity of liquid copper at multimegabar pressures, Phys. Rev. B **96**, 174109 (2017).

[43] M. P. Desjarlais, M. D. Knudson, and K. R. Cochrane *et al.*, Extension of the Hugoniot and analytical release model of α-quartz to 0.23 TPa, J. Appl. Phys. **122**, 035903 (2017).

[44] R. Trainor, Simple model for decay of laser generated shock waves, Techical Report, California University, Livermore (USA), Lawrence Livermore Laboratory, 1980.

[45] F. Cottet and J. P. Romain, Formation and decay of laser-generated shock waves, Phys. Rev. A **25**, 576 (1982).

[46] P. M. Celliers and M. Millot, Imaging velocity interferometer system for any reflector (VISAR) diagnostics for high energy density sciences, Rev. Sci. Instrum. **94**, 011101 (2023).

[47] C. Garban-Labaune, E. Fabre, C. E. Max, R. Fabbro, F. Amiranoff, J. Virmont, M. Weinfeld, and A. Michard, Effect of laser wavelength and pulse duration on laser-light absorption and back reflection, Phys. Rev. Lett. **48**, 1018 (1982).

[48] W. Rozmus, V. T. Tikhonchuk, and R. Cauble, A model of ultrashort laser pulse absorption in solid targets, Phys. Plasmas **3**, 360 (1996).

[49] J. F. Drake, P. K. Kaw, Y. C. Lee, G. Schmid, C. S. Liu, and M. N. Rosenbluth, Parametric instabilities of electromagnetic waves in plasmas, Phys. Fluids **17**, 778 (1974).

[50] J. K. Wicks, R. F. Smith, D. E. Fratanduono, F. Coppari, R. G. Kraus, M. G. Newman, J. R. Rygg, J. H. Eggert, and T. S. Duffy, Crystal structure and equation of state of Fe-Si alloys at super-Earth core conditions, Sci. Adv. **4**, eaao5864 (2018).